

Confined Hyperbolic Nanoridge Modes for Structured Illumination Microscopy

John Haug ^{Δ,*}, Milan Palei ^Δ, Joshua D. Shrout ^{↓,†}, Evgenii Narimanov [€], Paul W. Bohn ^{τ,⊥}, and Anthony J. Hoffman ^Δ

^Δ *Department of Electrical Engineering, University of Notre Dame, Notre Dame, IN 46556, USA*

[↓] *Department of Civil and Environmental Engineering and Earth Sciences, University of Notre Dame, Notre Dame, IN 46556, USA*

[†] *Department of Biological Sciences, University of Notre Dame, Notre Dame, IN 46556, USA*

[€] *Brick Nanotechnology Center, School of Computer and Electrical Engineering, Purdue University, West Lafayette, Indiana 47907*

[⊥] *Department of Chemistry and Biochemistry, University of Notre Dame, Notre Dame, IN 46556, USA*

^τ *Department of Chemical and Biomolecular Engineering, University of Notre Dame, Notre Dame, IN 46556, USA*

Supporting Information Placeholder

ABSTRACT: Plasmonic hyperbolic metasurfaces have emerged as an effective platform for manipulating the propagation of light. In this work, we leverage confined modes on arrays of silver nanoridges, which exhibit a hyperbolic-in-nature refractive index, to theoretically demonstrate and model a super-resolution imaging technique based on structured illumination microscopy. We demonstrate a spatial resolution of ~52 nm at 458 nm, which is 3.44 times better than an equivalent diffraction limited image. In addition, we demonstrate how the anisotropic properties of the metasurface dispersion can be leveraged to further improve the resulting spatial resolution to ~50 nm. This work emphasizes the ability to engineer the properties of confined optical modes and to leverage those characteristics for applications in imaging. The results of this work could lead to improved approaches for super-resolution imaging using designed sub-wavelength structures.

The desire to study and observe cellular and dynamic features of biological phenomena is a driving force behind improving the resolution limits of optical microscopy. For traditional optical microscopy, the resolution, Δx , is limited by the wavelength of light, λ , and the numerical aperture, NA , of the objective lens: $\Delta x \sim \frac{\lambda}{2NA}$.¹ For a typical imaging setup ($NA = 1.4$) and $\lambda = 550$ nm, a spatial resolution of approximately 220 nm can be achieved. This resolution is insufficient to observe many important sub-cellular structures, which exhibit spatial extents on the order of tens of nanometers or less.² To improve the spatial resolution, light with shorter wavelengths can be used; however, using this high-energy light to illuminate biological cells can damage or kill the specimens, limiting the ability to observe dynamical processes. Additionally, effects such as photobleaching can lead to deterioration of the cells, therefore masking their behavior in a natural environment.^{3,4} To overcome the resolution limits in traditional imaging instruments without resorting to shorter wavelength light, a variety of super-resolution techniques have been developed and demonstrated both analytically and experimentally, including but not limited to stochastic optical reconstruction microscopy (STORM)⁵, hyperlens imaging^{6,7}, and photoactivated localization microscopy.⁸

Among these techniques, structured illumination microscopy (SIM) is of particular interest for biological applications because in addition to producing super-resolution images, SIM is a wide-field imaging technique capable of higher imaging speeds that are needed for observation of cellular processes.⁹ Indeed, SIM has already been applied to *in vivo* biological imaging applications in a variety of animal cell samples, like zebrafish eyes, rabbit jejunum, and human lung fibroblasts.^{9,10}

The underlying principle of SIM is to capture high spatial frequency information by leveraging the Moiré effect between a structured illumination pattern and the object under investigation. The Moiré effect is a result of interference between two oscillating optical fields, which results in a low-spatial frequency pattern from the interference of the two higher spatial frequency inputs.^{11,12} SIM can improve the spatial resolution roughly two-fold compared to the diffraction limit.^{13,14} Variants of SIM, such as plasmonic structured illumination microscopy (PSIM) and localized plasmonic structured illumination microscopy (LPSIM), rely on the same principles, but leverage different optical phenomena to generate the illumination patterns. These approaches have achieved nearly 3x improved spatial resolution compared to traditional diffraction-limited wide-field images.¹⁵⁻¹⁸

Plasmonic structured illumination microscopy adapts traditional SIM techniques while utilizing excited surface plasmons polaritons (SPPs) as the structured illumination pattern in the imaging process.¹⁹ In comparison to traditional SIM techniques, the large wavevectors associated with surface plasmons ($|k_{sp}|$) improve the image resolution by as much as 2.6x with a single illumination wavelength of 532 nm.²⁰ More recently, building upon PSIM, Ponsetto *et. al* experimentally demonstrated LPSIM, utilizing localized plasmonic modes, excited on metallic nanodisc arrays, to surpass the previously demonstrated resolution limit of PSIM, achieving a spatial resolution of 75 nm, an improvement of ~3x with an illumination wavelength of 488 nm.^{21,22} Although utilizing structured illumination patterns of different origins, SIM, PSIM, and LPSIM, all utilize the Moiré effect and reconstruction algorithms to achieve super-resolution imaging.

In SIM, super-resolution images are constructed from multiple diffraction-limited images. Each diffraction-limited image is the result of the Moiré fringes produced and the collecting optics, where only light with wavevectors within the passband of the optical transfer function (OTF) can be detected. The OTF is represented in reciprocal space in Figure 1 as a dashed, grey circle of radius k_{cutoff} , where k_{cutoff} represents the maximum wavevector that can be resolved and is inversely related to the minimum spatial resolution that can be imaged in the far-field. Typical values of k_{cutoff} lie close to $\sim \frac{2NA}{\lambda}$. In SIM, wavevectors beyond k_{cutoff} are accessible through interference between an object and a structured illumination pattern with wavevectors of magnitude $k_{illumination}$. Thus, the maximum wavevector contributing to the reconstructed image can be as large as $k_{cutoff} + k_{illumination}$. The super-resolution image is obtained via a reconstruction algorithm that combines multiple overlapping images with different illumination phases and orientations.²³ This results in a resolution that is proportional to $\frac{1}{k_{cutoff} + k_{illumination}}$. When $k_{cutoff} \approx k_{illumination}$, the resolution improvement is close to a factor of 2. To further enhance the resolution, illumination patterns with large spatial wavevectors are needed. As mentioned previously, PSIM and LPSIM leverage the large wavevectors associated with SPP and LSPP modes to achieve their respective resolution enhancements.

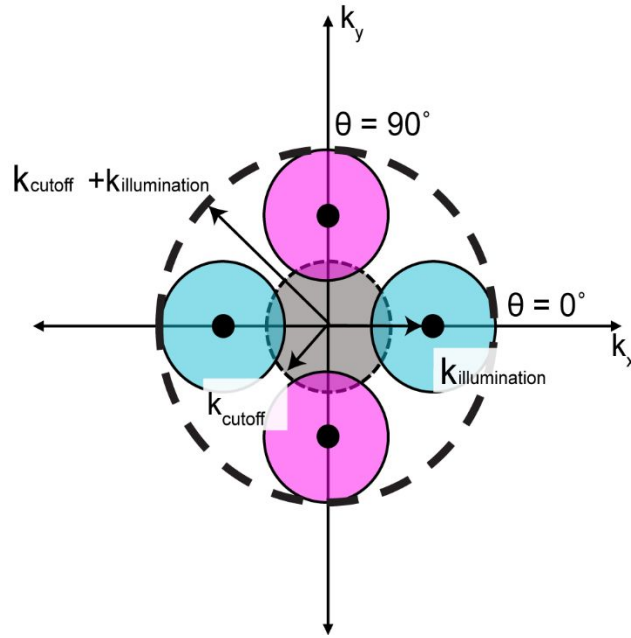


Figure 1. Fourier representation of the components of SIM. The gray circle of radius k_{cutoff} corresponds to the diffraction-limited PSF using conventional microscopy, and $k_{illumination}$ is the spatial frequency of the illumination pattern used. At different angles of orientation of the illumination pattern θ , the direction of the PSF frequency shift changes in Fourier space correspondingly.

In this work, we numerically demonstrate how improved super-resolution imaging can be achieved by engineering the effective index of confined optical modes. To achieve this, we use a patterned substrate comprised of coupled silver (Ag) nanoridge arrays that are engineered to exhibit hyperbolic dispersion. Surface plasmon polaritons on the narrow, closely-spaced ridges couple, resulting in optical modes with large wavevector, k_{hyp} . When localized, these high-k modes produce standing waves with spatial frequencies that exceed those of LSPPs, resulting in a resolution improvement at a single wavelength of 3.33x, compared to 3x for LSPIM. The resolution of our approach can be further improved by taking advantage of the optical anisotropy of the coupled ridge geometry; we demonstrate an additional improvement to 3.44x.

The structure consists of Ag ridges arrays surrounded by water as shown schematically in Fig. 2. Each ridge is 90 nm wide, 100 nm tall, and has length l . The ridges are separated both laterally and longitudinally by 90 nm. We use the SPP frequency of Ag, because the Ag-dielectric interface spans the entire visible spectrum with small loss. Water is used in the analysis, as it is a common medium for most biological cells. The ridge width and lateral separation are engineered to achieve hyperbolic dispersion in the spectral region near $\lambda_0 = 458$ nm, a wavelength selected because it corresponds to the fluorescence excitation maximum of flavins, which are important mediators of electron transfer as part of metabolism. Most bacterial species are known to incorporate flavin adenine dinucleotide (FAD) and/or flavin mononucleotide (FMN) as part of energy generating cascades in their membranes, which can serve as a prototypical bacteria for studying metabolic pathways.

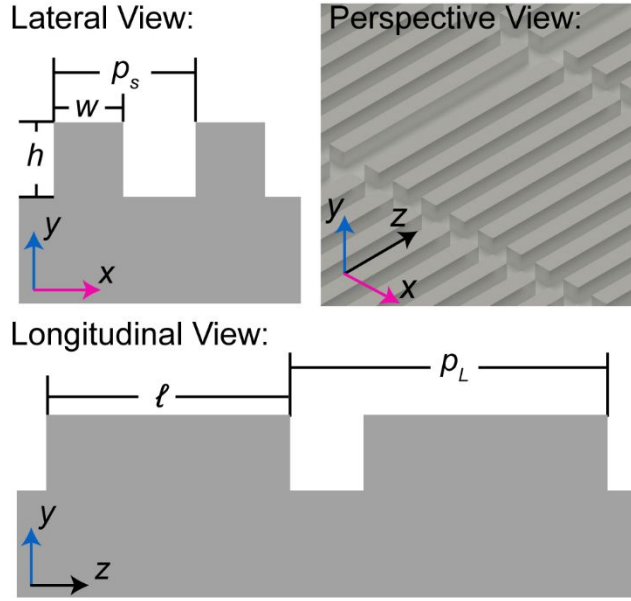


Figure 2. Schematic of the nanoridge structures studied in both lateral, x , and longitudinal, z , views, where w is the width, h is the height, and l is the length of the ridge. The periodicity in the lateral direction is p_s and in the longitudinal direction is p_L . The Perspective View shows an isometric view of the ridges with the corresponding coordinate system also provided (top right).

Figure 3(a) and (b) show the real and imaginary parts of the effective modal index of a coupled plasmonic mode. The electric field intensity distribution obtained using COMSOL Multiphysics eigenmode analysis is shown in Fig. 3(c). Here, $w = 90$ nm, $h = 100$ nm, and $p = 180$ nm (see Fig. 2), and the top semi-infinite space is filled with water. For these calculations, the permittivity of silver is interpolated from Ref. 24.²⁴ The effective modal index n_{eff} , where $k_{eff} = n_{eff} * k_0$, is shown for two different wavelengths ($\lambda_0 = 458$ nm and 750 nm). At $\lambda_0 = 458$ nm, the constant-frequency contour exhibits a maximum at $k_x = \pm\pi/p$ and a minimum at $k_x = 0$. This behavior is characteristic of a hyperbolic metasurface where the wavevector can become large with increasing k_x , and wave propagation is strongly anisotropic.²⁵⁻²⁷ Similar hyperbolic metasurfaces have already been shown to demonstrate negative refraction of optical surface waves.^{28,29} In comparison, for $\lambda_0 = 750$ nm the dispersion follows a convex frequency contour. Figure 3B depicts the imaginary part of the effective modal index, $Im(n_{eff})$.

The real and imaginary parts of the effective modal index for SPPs excited at a silver-water interface at $\lambda_0 = 458$ nm are also shown in Fig. 3 for comparison. To calculate the SPP modes at the silver-water interface, we use the same permittivity for silver and the dispersion is given by $|k_{spp}| = |k_{photon}| \left[\frac{\epsilon_m \epsilon_d}{\epsilon_m + \epsilon_d} \right]^{\frac{1}{2}}$ where $|k_{photon}|$ and $|k_{spp}|$ are the magnitude of the wavevectors for a free-space photon and the SPP, and ϵ_m and ϵ_d are the frequency-dependent permittivity of the metal and water, respectively.³⁰ Figure 3(A) compares the real part of the effective model index for modes on the nanoridges surrounded by water(magenta) and SPPs at a silver-water interface (black). The effective index for the coupled mode supported on the nanoridges at $k_x = 0$ is approximately 30% greater than the effective index for SPPs at a silver-water interface. The difference is even larger for $k_x \neq 0$. Standing waves can be created in both systems using structures with finite lengths, which can serve

as illumination patterns. The higher effective index for modes on the nanoridges will result in illumination patterns with higher spatial frequencies than those obtained using SPPs.

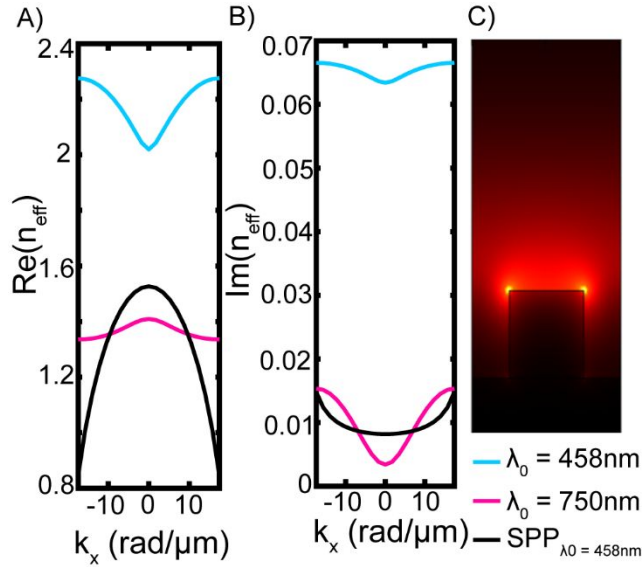


Figure 3. (A) Real and (B) imaginary parts of the effective modal index for SPPs propagating along silver-water interface (black) at the top of the silver nanoridges $\lambda_0 = 458\text{ nm}$ (blue) and $\lambda_0 = 750\text{ nm}$ (pink) with ($w = 90\text{ nm}$, $h = 100\text{ nm}$, and $p_s = 180\text{ nm}$). The dispersion is hyperbolic (concave) for $\text{Re}(n_{\text{eff}})$ when $\lambda_0 = 458\text{ nm}$ and convex for $\lambda_0 = 750\text{ nm}$. (C) Calculated electric field mode profile obtained using COMSOL eigenmode analysis for $\lambda_0 = 458\text{ nm}$ at $k_x = 0$.

At optical frequencies, metallic nanorod structures can act as one-dimensional Fabry-Perot resonators for confining surface plasmons.³¹ By modifying the length of the nanowire and the underlying substrate, the resonant mode frequency and electric field distribution can be engineered.^{32,33} Similarly, the length of the coupled ridges, ℓ , determines the frequency of supported resonant modes. We simulate arrays of silver nanoridges of varying length illuminated by plane waves using the commercial software package Lumerical. Here, we vary only the length of the ridges in the array, keeping the other parameters constant at $h = 100\text{ nm}$, $w = 90\text{ nm}$, $p_s = 180\text{ nm}$, $p_L = (90\text{ nm} + \ell)$, and $\lambda_0 = 458\text{ nm}$, with reference to Fig. 2. Figure 4 shows the calculated electric field magnitude along a ridge in the array for three different antenna lengths. As expected, increasing the length of the antenna results in additional antinodes. The distance between antinodes (or points of constant phase of the standing wave) is related to the effective modal index, n_{eff} , calculated using COMSOL.

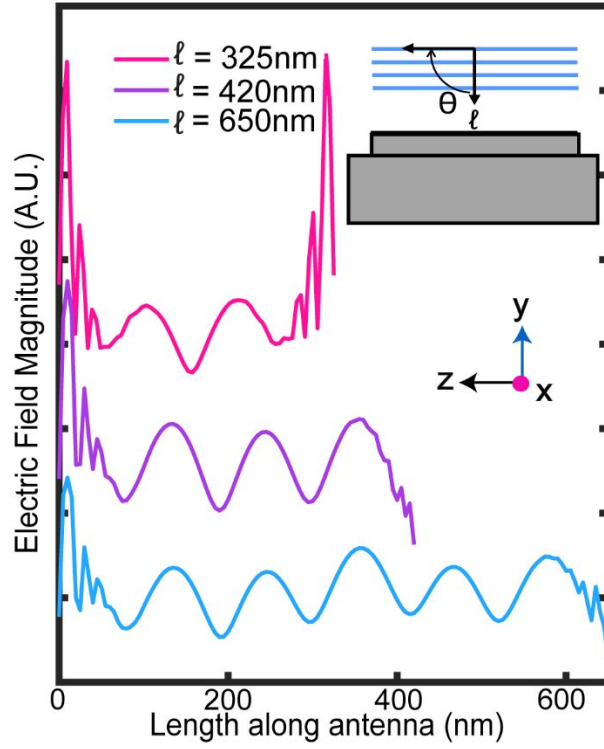


Figure 4. Electric field magnitude plotted along the length of three different lengths of nanoridges l (pink $l = 325$ nm, purple $l = 420$ nm, blue $l = 650$ nm) taken 5 nm above one of the top corners of the ridge, offset vertically for visibility. As the length of the nanoridges increases, the number of antinodes present along the top length of the nanoridges also increases. The parameters of the nanoridges are held constant at $w = 90$ nm, $h = 100$ nm, p_s at 180 nm, $p_L = l + 90$ nm, and the incident light is centered at $\lambda_0 = 458$ nm with an incident angle $\theta = 4^\circ$. A depiction of the illumination scheme is provided in the inset to the right of the figure, the incident light is p -polarized in this scheme.

To confirm that the mode present along the nanoantenna arrays is associated with the hyperbolic mode identified in the eigenmode calculations, we calculate the spatial frequency components of the electric field magnitude using Fourier analysis, Fig. 5(a). A peak at $55.58 \mu\text{m}^{-1}$ is observed, which arises from the periodicity of the electric field magnitude of the standing wave (Fig. 4). The eigenmode calculations predict an effective modal index of $n_{\text{eff}} = 2.019$ for $k_x = 0$. Treating the coupled nanoridge arrays of finite length as Fabry-Perot resonators with the calculated effective modal index, the predicted spacing between points of constant phase (e.g. peaks) in the electric field magnitude is 120 nm; this is in agreement with the field amplitude plots shown in Fig. 4. The vertical dashed line in Fig. 5A, corresponds to this frequency in the Fourier spectrum, showing excellent agreement between the eigenmode and plane-wave excitation calculations and supporting the assignment of the excited standing wave. The Fourier spectrum for confined SPP modes for 672.5 nm long antennas is also shown for comparison. As expected, the peak in the Fourier spectrum occurs at lower spatial frequencies.

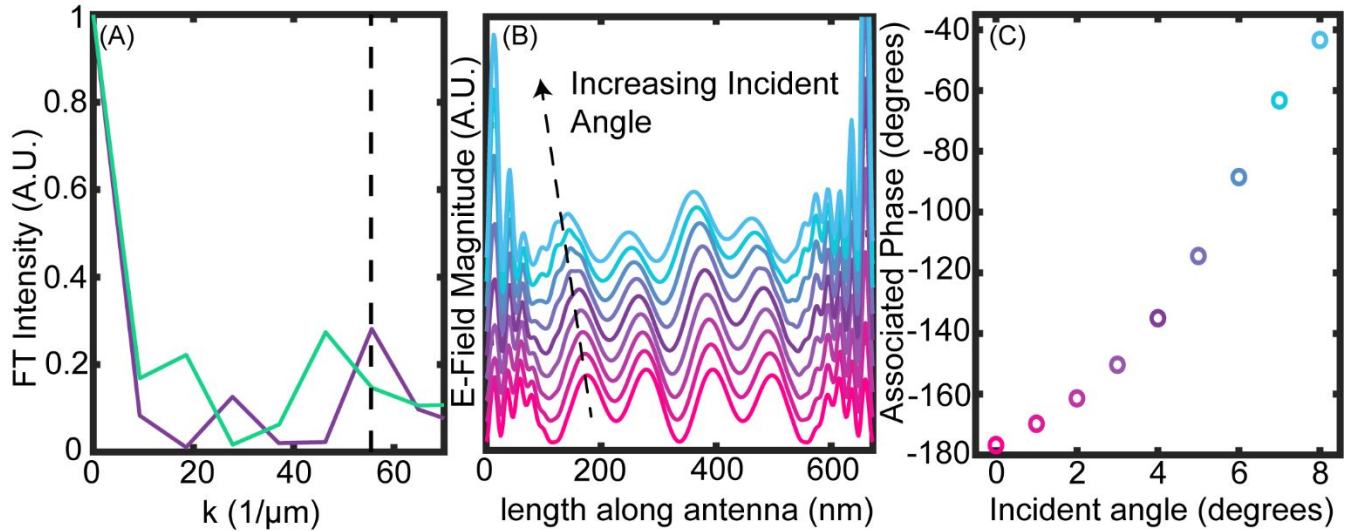


Figure 5. (A) Fourier spectrum of the electric field plot along the length of an $l = 672.5$ nm nanoridge (purple) at $\lambda_0 = 458$ nm at $\theta = 4$ degrees and a water-silver SPP (green) with the gray dashed line representing the frequency corresponding to the expected frequency of the $k_x = 0$ value for n_{eff} value from the mode analysis simulations shown in Fig. 4. (B) The electric field magnitude plotted along the length of $l = 672.5$ nm nanoridges at $\lambda_0 = 458$ nm at 9 different incident angles (0-8 degrees, following the pink to blue color transition), staggered vertically for visibility, taken 5 nm above the top corner structure. (C) The phase of the Fourier spectrum of the electric fields from (B) at the peak located near the expected hyperbolic frequency represented by the gray dashed line in (A).

The phase of the confined hyperbolic modes must be tunable in order to be utilized in SIM illumination. To demonstrate that the angle of incidence can be used to exert phase control over these hyperbolic modes, we calculate the electric field magnitude for several incident angles of 672.5 nm long antennas, ranging from normal incidence to 8° , as shown in Fig. 5(B). The phase of the electric field along the antennas clearly shifts. Figure 5(C) shows the phase of the Fourier transform for each of the incident angles, demonstrating a 130° shift that is monotonic with incident angle.

Finally, as a demonstration of the resolution enhancement possible using coupled ridge arrays, we adapt the opensource SIM code OpenSIM to simulate super-resolution images.³⁴ In these calculations, the full-width-half-maximum (FWHM) of the widefield point spread function (PSF) was 172 nm with the assumption that each pixel in the 2048 x 2048 pixel image represented 1 nm. We use a uniform sine wave as the illumination source. The spatial frequency and relationship between phase and incident angle are taken from the calculations shown in Fig. 5A and Fig. 5C, respectively. Using this scheme, we demonstrate a resolution enhancement in the reconstructed SIM image of distributed 9 nm diameter quantum dot emitters. Figure 6 shows three simulated images for the same distribution of quantum dots: a diffraction limited image with $NA = 1.4$ at $\lambda_0 = 458$ nm, Fig. 6(A); a SIM reconstructed image with an illumination pattern arising from localized silver-water SPPs at $\lambda_0 = 458$ nm, Fig. 6(B); and, a SIM reconstructed image with an illumination pattern arising from the coupled nanoridge arrays with $k_x = 8.727$ rad/ $\mu\text{m} = 0.5 \pi/p_s$; Fig. 6(C). In the SIM images, the wavevector of the incident light is always parallel to the longitudinal axis of the antenna arrays. Reconstructed images for both SIM approaches show significant improvements compared to the diffraction-limited image. Additionally, for closely spaced emitters, such as those in the center of the images, improved resolution of the coupled mode SIM image, Fig. 6(C) compared to that obtained with LPSIM, Fig. 6(B) is apparent. Figure 6(D) and Fig. 6(E) show the calculated intensity profile for a single quantum dot in each of the imaging scenarios.

Compared to the diffraction limited image, improvements of 2.8x, 3.3x, and 3.4x are observed for PSIM, coupled nanoridges with $k_x = 0$, and coupled nanoridges with $k_x = 8.727 \text{ rad}/\mu\text{m} = 0.5 (\pi/p_s)$, respectively. For the coupled nanoridge arrays analyzed here, the resolution improvement occurs along the longitudinal axis of the nanoridges; this is not necessarily true for LPSIM.^{21,22} However, it should be possible to design structures with higher degrees of rotational symmetry that leverage coupled plasmonic modes to improve resolution symmetrically in the plane.

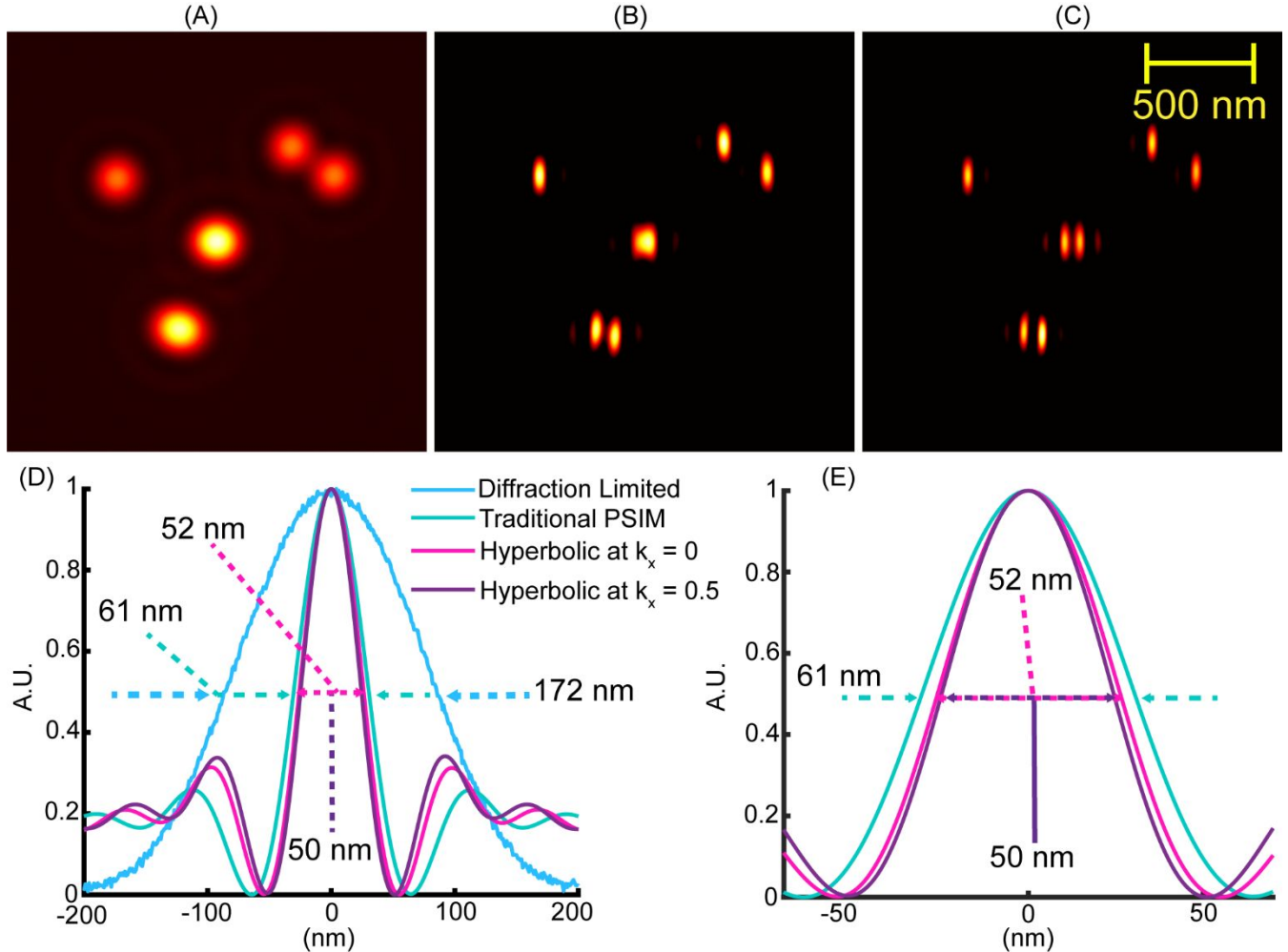


Figure 6. (A) Simulated diffraction limited wide-field image (2048x2048 pixels, each pixel representing 1 nm) for 6 quantum dots with 9 nm diameters randomly scattered with the center two dots being spaced 58 nm apart. (B) reconstructed appodized SIM image using a structured illumination pattern with frequency corresponding to the frequency we found via simulations for a silver-water SPP at $\lambda_o = 458 \text{ nm}$. (C) The reconstructed appodized image similar to (B) but now using our expected frequency for our hyperbolic nanoridges at $k_x = 8.727 \text{ rad}/\mu\text{m} = 0.5 (\pi/p_s)$. (D) Comparisons of the FWHM for a single quantum dot for the three cases in (A)-(C) as well as the FWHM for an illumination pattern corresponding to $k_x = 0$. (E) Expanded view of the center portion of the data plotted in (D).

In conclusion, we have numerically demonstrated that arrays of coupled plasmonic silver nanoridges can be engineered to confine modes with hyperbolic dispersion. This finding is particularly important for applications requiring imaging at a desired tunable wavelength. Our work shows how the super-resolution imaging system, in particular a structured illumination pattern, can be tailored for a particular wavelength and can improve spatial resolution in images to a degree that surpasses techniques based on plasmonic SIM and localized plasmonic SIM. Our simulations show that the resolution enhancement when using these structures with SIM is 3.44x compared to an equivalent diffraction-limited image. In addition to imaging with improved

resolution, the structures explored in this work are well-poised to explore bacterial aggregates and systems under electrochemical potential control.

Acknowledgements

This work was supported by the U.S. Department of Energy Office of Science through grant DE-SC0019312.

References

- (1) Heintzmann, R.; Ficz, G., Breaking the resolution limit in light microscopy. *Briefings in Functional Genomics* **2006**, *5* (4), 289-301.
- (2) Huang, B.; Bates, M.; Zhuang, X., Super-Resolution Fluorescence Microscopy. *Annual Review of Biochemistry* **2009**, *78* (1), 993-1016.
- (3) Magidson, V.; Khodjakov, A., Circumventing photodamage in live-cell microscopy. *Methods Cell Biol* **2013**, *114*, 545-60.
- (4) Lippincott-Schwartz, J.; Altan-Bonnet, N.; Patterson, G., Photobleaching and Photoactivation: Following Protein Dynamics in Living Cells. *Nature cell biology* **2003**, Suppl, S7-14.
- (5) Rust, M. J.; Bates, M.; Zhuang, X. Stochastic optical reconstruction microscopy (STORM) provides sub-diffraction-limit image resolution. *Nat. Methods* **2006**, *3*, 793–796.
- (6) Lu, D.; Liu, Z. Hyperlenses and Metalenses for Far-Field SuperResolution Imaging. *Nat. Commun.* **2012**, *3*, 1205.
- (7) Wan, W.; Ponsetto, J. L.; Liu, Z. Numerical Study of Hyperlenses for Three-Dimensional Imaging and Lithography. *Opt. Express* **2015**, *23*, 18501–18510.
- (8) Betzig, E.; Patterson, G. H.; Sougrat, R.; Lindwasser, O. W.; Olenych, S.; Bonifacino, J. S.; Davidson, M. W.; Lippincott-Schwartz, J.; Hess, H. F. Imaging Intracellular Fluorescent Proteins at Nanometer Resolution. *Science* **2006**, *313*, 1642–1645.
- (9) Ströhl, F.; Kaminski, C. F. Frontiers in Structured Illumination Microscopy. *Optica* **2016**, *3*, 667.
- (10) Mudry, E.; Belkebir, K.; Girard, J.; Savatier, J.; Le Moal, E.; Nicoletti, C.; Allain, M.; Sentenac, A. Structured illumination microscopy using unknown speckle patterns. *Nat. Photonics* **2012**, *6*(5), 312–315.
- (11) Yokozeki, S. Theoretical Interpretation of the Moiré Pattern. *Opt. Commun.* **1974**, *11* (4), 378 –381.
- (12) Bryngdahl, O. Moiré: formation and interpretation. *J. Opt. Soc. Am.*, **1974**, *64* (10), 1287 –1294.
- (13) Gustafsson, M. G. L.; Agard, D. A.; Sedat, J. W. Doubling the Lateral Resolution of Wide-Field Fluorescence Microscopy using Structured Illumination. *Proc. SPIE* **2000**, 3919, 141–150
- (14) Gustafsson, M. G. L. Surpassing the Lateral Resolution Limit by a Factor of Two Using Structured Illumination Microscopy. *J. Microsc.* **2000**, *198*, 82–87.
- (15) Frohn, J. T.; Knapp, H. F.; Stemmer, A. True optical resolution beyond the Rayleigh limit achieved by standing wave illumination. *Proc. Natl. Acad. Sci. U.S.A.* **2000**, *97*, 7232–7236.
- (16) Tan, O.; Xu, Z.; Zhang, D.H.; Yu, T.; Zhang, S.; Luo, Y. Polarization-Controlled Plasmonic Structured Illumination *Nano Letters* **2020** *20* (4), 2602-2608.
- (17) Bezryadina, A.; Zhao, J.; Xia, Y.; Zhang, X.; Liu, Z. High Spatiotemporal Resolution Imaging with Localized Plasmonic Structured Illumination Microscopy. *ACS Nano* **2018**, *12* (8), 8248-8254.
- (18) Schermelleh, L.; Carlton, P. M.; Haase, S.; Shao, L.; Winoto, L.; Kner, P.; Burke, B.; Cardoso, M. C.; Agard, D. A.; Gustafsson, M. G. L.; Leonhardt, H.; Sedat, J. W. Subdiffraction multicolor imaging of the nuclear periphery with 3D structured illumination microscopy. *Science* **2008**, *320*, 1332–1336.
- (19) Wei, F.; Liu, Z. Plasmonic Structured Illumination Microscopy. *Nano Lett.* **2010**, *10* (7), 2531-2536.
- (20) Wei, F.; Lu, D.; Shen, H.; Wan, W.; Ponsetto, J. L.; Huang, E.; Liu, Z. Wide Field Super-Resolution Surface Imaging through Plasmonic Structured Illumination Microscopy. *Nano Lett.* **2014**, *14*, 4634–4639.
- (21) Ponsetto, J. L.; Wei, F.; Liu, Z. Localized plasmon assisted structured illumination microscopy for wide-field high-speed dispersion-independent super resolution imaging. *Nanoscale*, **2014**, *6*, 5807-5812.
- (22) Ponsetto J. L.; Bezryadina, A.; Wei, F.; Onishi, K.; Shen, H.; Huang, E.; Ferrari, L.; Ma, Q.; Zou, Y.; Liu, Z. Experimental Demonstration of Localized Plasmonic Structured Illumination Microscopy. *ACS Nano* **2017**, *11*(6), 5344-5350.
- (23) Heintzmann, R.; Huser, T., Super-Resolution Structured Illumination Microscopy. *Chemical Reviews* **2017**, *117* (23), 13890-13908.
- (24) Johnson, P. B.; Christy, R. Optical Constants of Noble Metals. *Phys. Rev. B* **1972**, *6*, 4370-4376.
- (25) Poddubny, A.; Iorsh, I.; Belov, P.; Kivshar, Y., Hyperbolic metamaterials. *Nature Photonics* **2013**, *7* (12), 948-957.
- (26) Boltasseva, A.; Atwater, H. A., Low-Loss Plasmonic Metamaterials. *Science* **2011**, *331* (6015), 290.
- (27) Hoffman, A. J.; Alekseyev, L.; Howard, S. S.; Franz, K. J.; Wasserman, D.; Podolskiy, V. A.; Narimanov, E. E.; Sivco, D. L.; Gmachl, C., Negative refraction in semiconductor metamaterials. *Nature Materials* **2007**, *6* (12), 946-950.
- (28) Liu, Y.; Zhang, X. Metasurfaces for manipulating surface plasmons. *Applied Physics Letters* **2013**, *103*, 141101.
- (29) High, A. A.; Devlin, R. C.; Dibos, A.; Polking, M.; Wild, D. S.; Perczel, J.; de Leon, N. P.; Lukin, M. D.; Park, H. Visible-frequency hyperbolic metasurface. *Nature* **2015**, *522*, 192-196.
- (30) Barnes, W. L.; Dereux, A.; Ebbesen, T. W. Surface Plasmon Subwavelength Optics. *Nature* **2003**, *424*, 824–830.
- (31) Cubukcu, E.; Capasso, F. Optical nanorod antennas as dispersive one-dimensional Fabry-Perot resonators for surface plasmons. *Appl. Phys. Lett.* **2009**, *95*, 201101.
- (32) Dominguez, O.; Nordin, L.; Lu, J.; Feng, K.; Wasserman, D.; Hoffman, A. J., Monochromatic Multimode Antennas on Epsilon-Near-Zero Materials. *Advanced Optical Materials* **2019**, *7* (10), 1800826.
- (33) Kim, J.; Dutta, A.; Naik, G. V.; Giles, A. J.; Bezares, F. J.; Ellis, C. T.; Tischler, J. G.; Mahmoud, A. M.; Caglayan, H.; Glembocki, O. J.; Kildishev, A. V.; Caldwell, J. D.; Boltasseva, A.; Engheta, N., Role of epsilon-near-zero substrates in the optical response of plasmonic antennas. *Optica* **2016**, *3* (3), 339-346.
- (34) Lal, A.; Shan, C.; Xi, P. Structured illumination microscopy image reconstruction algorithm. *IEEE J. Sel. Topics Quantum Electron* vol. *200 Jul./Aug.* **2016**, *4*, 50-63.